UNIVERSITY OF UTRECHT

DEBYE INSTITUTE

QUANTUM NANOPHOTONICS GROUP

Effect of Damping on Stability of Gold Nanoparticles in a Quadrupole Trap

Author:
James Findley de Regt

Supervisor:
Dr Dries van Oosten

July 18, 2016

Abstract

This thesis describes the use of time-varying quadrupole electric fields to trap gold nanospheres. Colloidal particles, $100\,\mathrm{nm}$ in diameter are extracted from their solution and injected into the trap via electrospray. The particles' response is studied at atmosphere as well as in a medium vacuum. A perturbing frequency is introduced alongside the main trapping frequency to allow the particles' response to resonant frequencies to be studied. Nonlinearities in the particles' response are discussed.

Contents

1 Introduction

This thesis describes the development of a trap based on the quadrupole ion trap (QIT). The trap was used to study the behaviour and features of gold nanoparticles. This thesis forms part of a greater project that aims to investigate the interaction of femtosecond laser pulses with various materials under ablation conditions.

1.1 The Quadrupole Ion Trap

The electric field schema which underpins the QIT was developed as a focusing technique for particle accelerators in the late 1940s and early 1950s. This technique, called strong focusing, relies on passing a particle beam through alternating electric fields to focus the beam along orthogonal axes. The technique was first developed by Christofilos, who filed a patent in 1950 [1]. The first published work in this emerging field, by Courant, Livingston, and Snyder in 1952 [2], describes the usage of strong focusing to construct a more efficient synchrotron. The seminal description of strong focusing as a trapping principle came from Wolfgang Paul in 1953 [3], a development for which he shared the 1989 Nobel Prize.

The QIT is, however, not only used for trapping. The particle's confinement within the trap is predicated by the particle's charge-to-mass ratio. Via a careful adjustment of the confinement parameters, particles will be ejected from the trap based on their charge-to-mass ratio, while other particles are left stably trapped [4]. This allows the QIT to be used as a mass spectrometer.

1.2 Description of Motivation

This thesis is written as preparatory work for future ablation experiments. Other experiments are done in parallel to this work. Refer to the work by Scholten [5], Clarijs [6], and Zomer [7] for more details of these other experiments. Trapping conductive nanometre-sized particles in free space would allow them to be studied without the effects related to a deposition substrate.

Ablation is the process of removing material from a surface. Laser ablation accomplishes this at low powers via evaporation, and at high powers by direct plasma conversion. The process of direct plasma conversion is an active area of research [8] [9]. Spherical, nanometre-sized targets reduce the dimensionality of the problem. Due to the small size, the distribution of transient material properties is essentially reduced to a constant over the ablation time line. This makes modelling and numerical simulations considerably less complex.

For these reasons, we set out to trap gold nanoparticles in a quadrupole trap.

1

2   Theory

This section describes the theory involved in trapping nanoparticles. The nanoparticles are extracted from a colloidal gold suspension via an electrospray process. The extracted nanoparticles are then trapped using time-varying electric fields from quadrupole electrodes. The effects of atmosphere on this trapping system are also discussed.

2.1   Colloids and Electrospray

A colloidal fluid is any solvent with nanoparticles suspended in it, where the nanoparticles do not significantly dissolve in the solvent. These nanoparticles are typically between the sizes of $1\,\mathrm{nm}$ and $1\,\mathrm{\mu m}$ [10].

We choose to use colloidal nanoparticles for this thesis because they meet the qualifications described in Sec. 1.2. Additionally, these particles are manufactured to reliable tolerances, and easy to acquire. Refer to Sec. 3.1 for details of the specific nanoparticles used for this thesis.
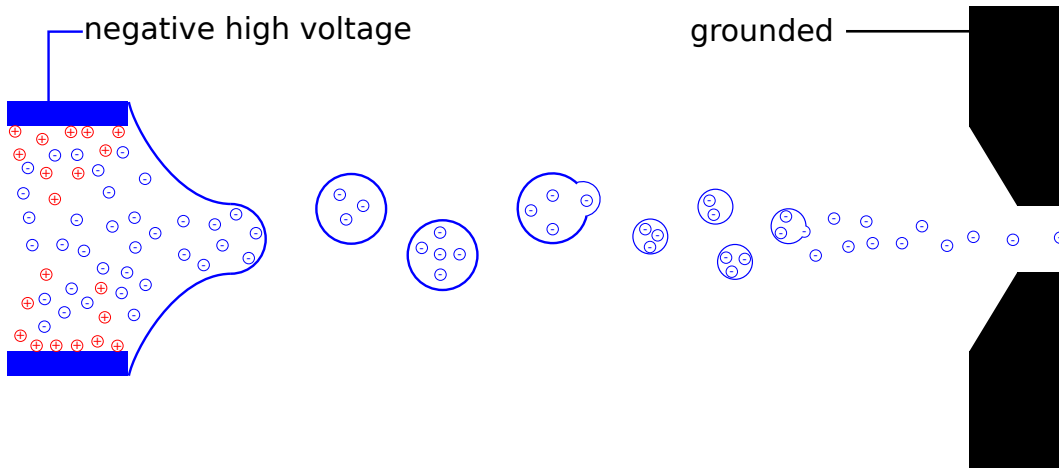

Figure 2.1: Schematic showing the electrospray process.

Electrospraying involves the aerosolization of a liquid by method of Coulomb repulsion. This is accomplished by applying high voltage to a volume of liquid, with an aperture for the volume to expand through.

The volume of liquid will form a droplet at the aperture, with surface tension across the droplet defined by the viscosity of the liquid, the size of the aperture, and the pressure of the backing volume. By adjusting the volume pressure together with the high voltage, it is possible to overcome the surface resistance of the liquid droplet at the aperture.

The droplet then breaks apart, aerosolizing, due to the Coulomb repulsion felt by the ions in the liquid. Refer to Fig. 2.1 for a schematic diagram of the electrospray process.

In general, a droplet of liquid with surface tension γ, radius r and electric permittivity ϵ will hold some charge q. A limit on the charge, q_r, beyond which the surface tension is overcome, was experimentally identified by Lord Rayleigh [11]. This Rayleigh limit is defined as

$$q_r = 8\pi\epsilon^{1/2}\gamma^{1/2}r^{3/2}. \tag{2.1}$$

In this thesis, the droplet is formed at the end of a thin tube, and the charge comes from a potential difference between an applied electric field in the fluid and an anode plate. The electric field then will be

$$E = \frac{2V}{R\ln(2d/R)}, \tag{2.2}$$

where V is the applied voltage, R the radius of the aperture, and d the distance to the anode [12]. Picking values for these three variables that approach the Rayleigh limit will cause the droplet to deform. This will typically take the form of a cone, known as the Taylor Cone. Refer to Fig. 2.2 for images of the Taylor cone.
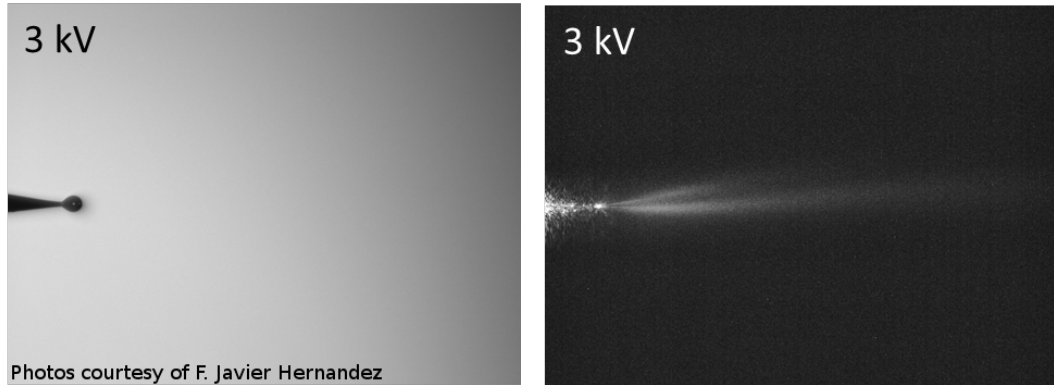

Figure 2.2: Droplet at the end of a needle tip, under an applied voltage of $3\,\mathrm{kV}$. The Taylor cone forms at the needle tip, followed by the electrospray.

At the Rayleigh limit the electrostatic repulsion overcomes the surface tension, and the tip of the cone will elongate until a droplet is ejected towards the anode. This droplet will eject further progeny droplets, aerosolizing and evaporating to the point where only the gold nanoparticles are left.

Refer to Sec. 3.1 for experimental details of the electrospray construction.

2.2   The Paul Trap

It has long been known that electrostatic forces alone cannot be used to confine a charged particle in free space [13]. This issue is typically resolved by the addition of a magnetic field, creating a Penning Trap [14], or by varying the electric fields in time, creating a Paul Trap [3]. The Paul Trap relies on switching the electric fields between electrodes more quickly than the particle can escape the trap. This causes a time-averaged stability, despite the trap being unstable in at least one axis at any particular time. It does this by generating a multi-pole field, and then switching the field between opposite poles. A quadrupole is the simplest version of this method.
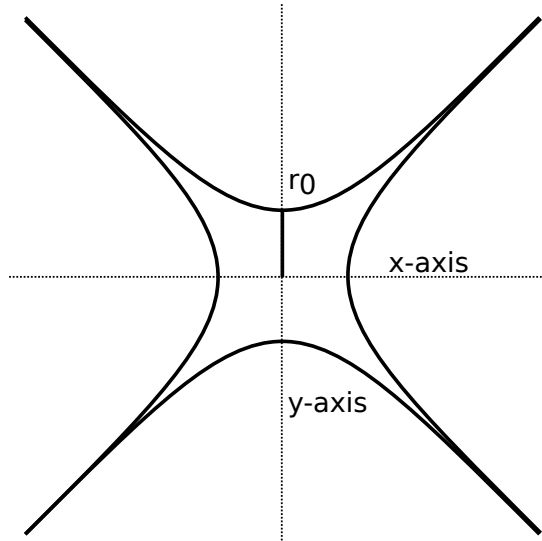

Figure 2.3: Schematic of the quadrupole trap. The hyperbolae represent the electrodes. The minimum distance from the central trap axis to the rod surface is given as r_0. The axes can be defined in any orientation.

The following derivation largely follows March [15] before introducing corrections discussed in Hasegawa et al. [16]. For an idealized test particle in a quadrupole trap, the potential $\phi(x, y, z)$ within the device is

$$\phi(x, y, z) = A(\lambda x^2 + \sigma y^2 + \gamma z^2) + C, \tag{2.3}$$

where A describes the potential between opposite electrodes and C is a fixed term applying to all electrodes. λ, σ and γ are weighting constants. Note that x-, y- and z-motions are all independent. Any electric field must satisfy the Laplace condition, $\nabla^2 \phi = 0$. Applying this to Eq. (2.3) yields

$$\nabla^2\phi = \frac{\partial^2\phi}{\partial x^2} + \frac{\partial^2\phi}{\partial y^2} + \frac{\partial^2\phi}{\partial z^2} = 0, \tag{2.4}$$

with these partial derivatives taking the form

$$\frac{\partial\phi}{\partial x} = \frac{\partial}{\partial x}(A\lambda x^2) = 2A\lambda x. \tag{2.5}$$

Their second derivatives work out to

$$\frac{\partial^2\phi}{\partial x^2} = 2\lambda A, \qquad \frac{\partial^2\phi}{\partial y^2} = 2\sigma A, \qquad \frac{\partial^2\phi}{\partial z^2} = 2\gamma A. \tag{2.6}$$

Substituting Eq. (2.6) into Eq. (2.4) yields

$$\nabla^2\phi = A(2\lambda + 2\sigma + 2\gamma) = 0, \tag{2.7}$$

and since A is a non-zero term, 2.7 becomes

$$\lambda + \sigma + \gamma = 0. \tag{2.8}$$

For a two-dimensional system, we choose the lowest order solution, where

$$\lambda = -\sigma = 1; \qquad \gamma = 0. \tag{2.9}$$

Substituting Eq. (2.9) into Eq. (2.3) gives

$$\phi(x, y, 0) = \phi(x, y) = A(x^2 - y^2) + C. \tag{2.10}$$

To determine the constants A and C, we will now consider the form of the field from a hyperbolic rod. A quadrupole trap has two sets of rods, with the equations

$$\frac{x^2}{x_0^2} - \frac{y^2}{a^2} = 1, \qquad \frac{x^2}{b^2} - \frac{y^2}{y_0^2} = 1, \tag{2.11}$$

for the x- and y-rods, corresponding respectively to the conditions $x = \pm x_0$ for $y = 0$ and $y = \pm y_0$ for $x = 0$. For the quadrupole potential to be formed correctly, the hyperbolae must share common asymptotes, such that $a = \pm x$ and $b = \pm y$. In practice, nearly all QIT devices are built such that a circle with radius r_0 can be

inscribed tangentially to the nearest surface of each electrode, such that the equations describing the electrode surfaces become

$$x^2 - y^2 = r_0^2, \qquad x^2 - y^2 = -r_0^2, \tag{2.12}$$

for the x- and y-electrodes respectively.

In this two dimensional set-up, particles enter the QIT along the z-axis, and react to the switching electric fields with some small oscillations along the x- and y-axes. This is referred to as the secular oscillation, and depends on the particle charge-to-mass ratio. All particles with similar charge-to-mass ratios will experience the same secular frequency whilst in the trap.

The potential described in Eq. (2.3) results from the difference between the potentials applied to the x- and y-rod sets, $\phi_0 = \phi_x - \phi_y$. Considering the rod sets individually, ϕ_x and ϕ_y are defined as

$$\phi_x = A(r_0^2) + C, \quad \text{and} \quad \phi_y = A(-r_0^2) + C. \tag{2.13}$$

Note that C is a fixed term representing a direct current (DC) offset from ground. For the rest of this derivation it shall be set to zero. Combining the two ϕ terms gives

$$\phi_0 = 2Ar_0^2, \qquad A = \frac{\phi_0}{2r_0^2}. \tag{2.14}$$

Thus, Eq. (2.10) becomes

$$\phi(x,y) = \frac{\phi_0}{2r_0^2}(x^2 - y^2). \tag{2.15}$$

Now consider a test particle subjected to this potential. Setting the y-component to zero gives

$$\phi(x,0) = \frac{\phi_0 x^2}{2r_0^2}. \tag{2.16}$$

The field at point $(x, y = 0)$ is then

$$\frac{\partial \phi(x,0)}{\partial x} = \frac{\phi_0 x}{r_0^2}, \tag{2.17}$$

and the resulting electrical force acting on the test particle is

$$F_x = -e\frac{\partial \phi(x,0)}{\partial x} = -e\frac{\phi_0 x}{r_0^2}, \tag{2.18}$$

where the e has a minus because the forces fall off in intensity away from the center. Assuming this force is the predominant cause of motion, Newton's second law produces

$$-m\left(\frac{d^2 x}{dt^2}\right) = -e\frac{\phi_0 x}{r_0^2}. \tag{2.19}$$

Consider a periodic potential, of the form

$$\phi_0 = 2(U + V\cos\Omega t), \tag{2.20}$$

where U is a DC voltage, applied with opposite polarities to the x- and y-electrodes. V is a zero-to-peak alternating current (AC) voltage, with Ω as its frequency. Combining these two equations creates

$$m\left(\frac{d^2 x}{dt^2}\right) = -2e\frac{(U + V\cos\Omega t)x}{r_0^2}. \tag{2.21}$$

For future convenience, 2.21 can be rewritten as

$$\left(\frac{d^2 x}{dt^2}\right) = -\left[\frac{2eU}{mr_0^2} + \frac{2eV\cos\Omega t}{mr_0^2}\right]x. \tag{2.22}$$

2.3   The Mathieu Equation

The traditionally expressed [17] form of the Mathieu equation is

$$\frac{d^2 u}{d\xi^2} + (a_u - 2q_u\cos 2\xi)u = 0, \tag{2.23}$$

where u is a displacement, and ξ is a dimensionless parameter equal to $\frac{\Omega t}{2}$. The parameters a_u and q_u are dimensionless stability parameters. These parameters describe boundaries where the equation produces stable results. Solving for them gives insight into what physical properties are important for stable trapping. If one considers the first and second order derivatives of ξ

$$\frac{d}{dt} = \frac{d\xi}{dt}\frac{d}{d\xi} = \frac{\Omega}{2}\frac{d}{d\xi}, \tag{2.24}$$

and

$$\frac{d^2}{dt^2} = \frac{d\xi}{dt}\frac{d}{d\xi}\left[\frac{d}{dt}\right] = \frac{\Omega^2}{4}\frac{d^2}{d\xi^2}, \tag{2.25}$$

this leads to

$$\frac{d^2u}{dt^2} = \frac{\Omega^2}{4}\frac{d^2u}{d\xi^2}. \tag{2.26}$$

Now, substituting Eq. (2.26) into Eq. (2.23)

$$\frac{d^2u}{dt^2} = -\left[\frac{\Omega^2}{4}a_u - 2 \times \frac{\Omega^2}{4}q_u\cos\Omega t\right]u, \tag{2.27}$$

leads to combining Eq. (2.27) with Eq. (2.22)

$$-\left[\frac{2eU}{mr_0^2} + \frac{2eV\cos\Omega t}{mr_0^2}\right]u = -\left[\frac{\Omega^2}{4}a_u - \frac{\Omega^2}{2}q_u\cos\Omega t\right]u, \tag{2.28}$$

to describe the u-displacement of the test particle in the trap. Solving for a_u and q_u

$$a_x = \frac{4eU}{mr_0^2\Omega^2}, \qquad q_x = -\frac{2eV}{mr_0^2\Omega^2}, \tag{2.29}$$

where e is the charge and m is the mass of the test particle, r_0 is the minimum distance from trap center to the surface of the electrodes. U is a DC voltage applied with opposite polarities to the electrode sets, and V a zero-to-peak AC voltage with Ω as its frequency.

Refer to Fig. 2.4 for a diagram of the Mathieu equation stability parameters. This diagram shows both the x- and z-axis stability zones, as well as the overlapping zone where there is two-axis stability.

2.4   Atmospheric corrections to the Mathieu Equation

Atmospheric damping is accounted for by adding a friction term to Eq. (2.22)
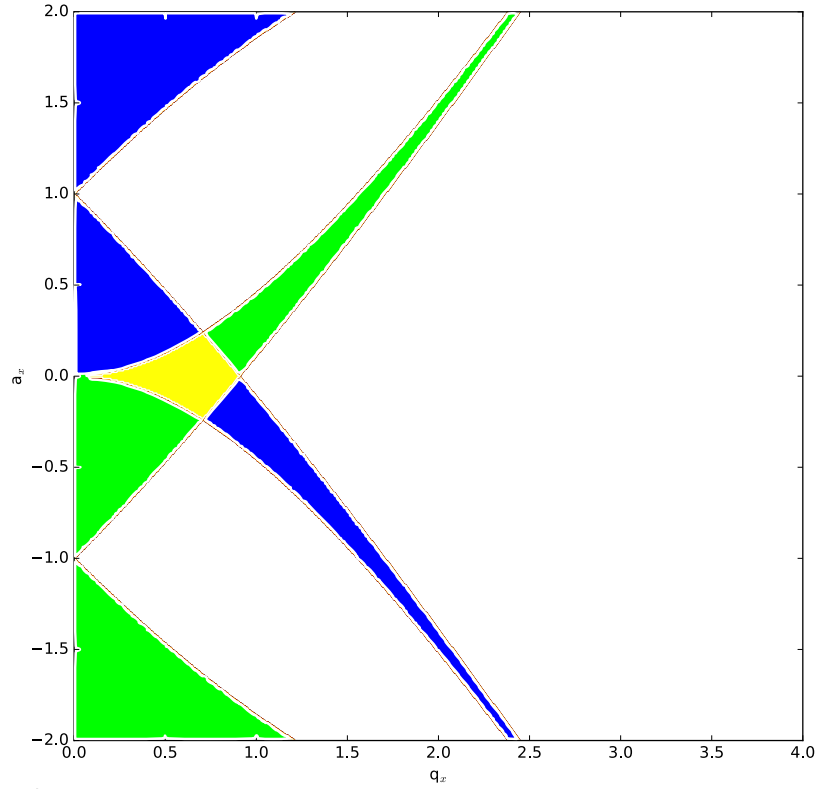
Figure 2.4: The Mathieu equation stability parameters q and a against each other. The lines indicate the boundaries of the stable regions. The blue zone indicates stability along the x-axis, and the green zone along the z-axis. The yellow region is the overlap between two regions, and thus is the only stable region along both axes.

$$\left(\frac{d^2x}{dt^2}\right) + \frac{\beta}{m}\frac{dx}{dt} + \left[\frac{2eU}{mr_0^2} + \frac{2eV\cos\Omega t}{mr_0^2}\right]x = 0. \tag{2.30}$$

Similarly to Sec. 2.3, the variable ξ accounts for the time component

$$\xi = \frac{\Omega t}{2}, \qquad t = \frac{2\xi}{\Omega}, \qquad \frac{\partial}{\partial t} = \frac{\Omega}{2}\frac{\partial}{\partial\xi}, \qquad \frac{d^2}{dt^2} = \frac{\Omega^2}{4}\frac{d^2}{d\xi^2}. \tag{2.31}$$

This allows Eq. (2.30) to be rewritten as

$$\left(\frac{d^2x}{d\xi^2}\right) + \frac{2\beta}{m\Omega}\frac{dx}{d\xi} + \left[\frac{4eU}{m\Omega^2 r_0^2} + \frac{4eV\cos\Omega 2\xi}{m\Omega^2 r_0^2}\right]x = 0. \tag{2.32}$$

Now, the same a and q parameters defined in Eq. (2.29) are joined by an additional variable κ

$$\kappa = \frac{\beta}{m\Omega}, \tag{2.33}$$

permitting the Mathieu equation of Eq. (2.23) to be rewritten as

$$\frac{d^2u}{d\xi^2} + 2\kappa\frac{du}{d\xi} + (a_u - 2q_u\cos 2\xi)u = 0. \tag{2.34}$$

The variable β is still not defined, so now the form of damping the particle will experience must be considered. The nanoparticle, in its secular motion perpendicular to the trap axis, will encounter the residual gas left in the vacuum chamber. The friction from this produces drag. First, what sort of drag this is must be established. The Knudsen number is a measure of the relative size of a test particle to the length scale of the problem, and is given by

$$\mathrm{Kn} = \frac{\ell_{\mathrm{mfp}}}{a}, \tag{2.35}$$

where a is a typical length of the test particle, in this case the diameter, and ℓ_{mfp} is the mean free path of the fluid. a for these particles is $100\,\mathrm{nm}$. The vacuum was typically in the order of $10\,\mathrm{Pa}$, where the ℓ_{mfp} of air is $690\,\mathrm{\mu m}$. This gives a Knudsen number of 6900.

A small spherical test particle in a viscous fluid will experience resistance described by Stoke's Law [18]. However, Stoke's Law assumes a viscous particle-fluid boundary with no relative flow. In the case of high Knudsen numbers, this is not the case. One can use the Cunningham correction factor to account for this slippage [19]

$$C = 1 + 2\mathrm{Kn} + \left(A_1 + A_2 \cdot e^{\frac{-A_3}{\mathrm{Kn}}}\right). \tag{2.36}$$

The values of A_1, A_2, and A_3 have been experimentally determined for air [20]

$$A_1 = 1.257, \qquad A_2 = 0.400, \qquad A_3 = 0.55. \tag{2.37}$$

Thus the corrected Stoke's Law is

$$\mathbf{F} = \frac{6\pi a\eta\mathbf{V}}{C}, \tag{2.38}$$

where a is the particle radius, η the viscosity of the fluid, $\mathbf{V}$ the fluid's motion relative to the particle, and C is the Cunningham correction factor.

Now, if β is defined as

$$\beta = \frac{6\pi a\eta}{C}, \tag{2.39}$$

then κ as defined in Eq. (2.33) accounts for the drag experienced from air resistance, and is unit-less.

Refer to Fig. 2.5 for diagrams of the atmosphere-corrected stability zones. The rows, upper and lower, show the diagrams for normal operating pressures and for atmosphere respectively. The columns, left and right, show the diagrams for a smaller and larger test particle respectively. Note that the normal operating pressure diagrams are essentially indistinguishable from each other, and from Fig. 2.4. For small values of κ this correction is very minor. However, the diagrams for atmospheric pressure clearly indicate the dominance of the κ term. Additionally, the size of the test particle plays a much smaller role in higher vacuums. Again, there is practically no difference visible between the two test particles at operating pressures. Yet, at atmosphere, the larger test particle has a clearly broader stability zone.
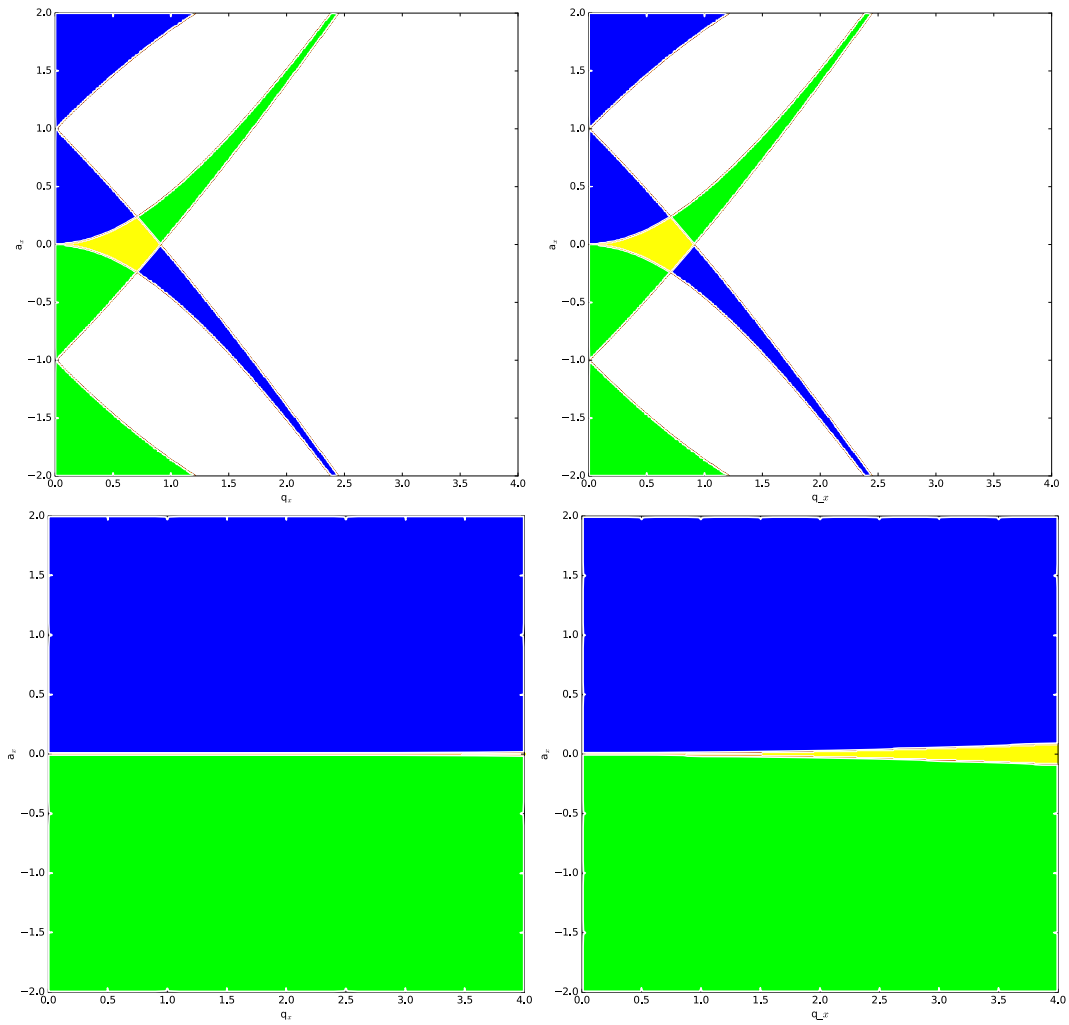
Figure 2.5: The Mathieu equation atmosphere corrected stability parameters q and a
against each other. The blue zone indicates stability along the x-axis, and the green zone
along the z-axis, and the yellow region is the stable region along both axes.
The upper row shows the diagrams for $20\,\mathrm{Pa}$, and the lower row for normal atmosphere.
The right column of diagrams is for particle radius $50\,\mathrm{nm}$, and the left for $150\,\mathrm{nm}$.

3   Experiment Design

The purpose of this section is to describe the individual components of the experimental apparatus, and how they are used to perform the experiments. All of the work in this set of experiments begins by extracting gold nanoparticles from a colloidal suspension and injecting them via electrospray into the quadrupole trap. Refer to the report by N. D. Kosters [21] for the work done prior to this thesis.

3.1   Nanoparticles and Electrospray

We use a colloidal suspension of gold nanoparticles from NanoComposix, product number AUPN100. The particles in this suspension are gold spheres with a diameter 100 ± 5 nm, coated in polyvinylpyrrolidone (PVP), and suspended in water at a concentration of 0.05 mg/mL. PVP is a surfactant, chosen because it reduces particle aggregation and is stable across a wide variety of solvents. PVP acquires a negative charge at neutral pH, producing a repulsive force between the nanoparticles.

Samples from this suspension were further diluted with ethanol at ratios determined by the particular experiment. Where filtering is required, this is accomplished using millipore syringe filters, with a pore size of 0.22 µm. Prior to use, the sample of ethanol and colloidal suspension together was left in an ultrasonic bath for periods not longer than five minutes.
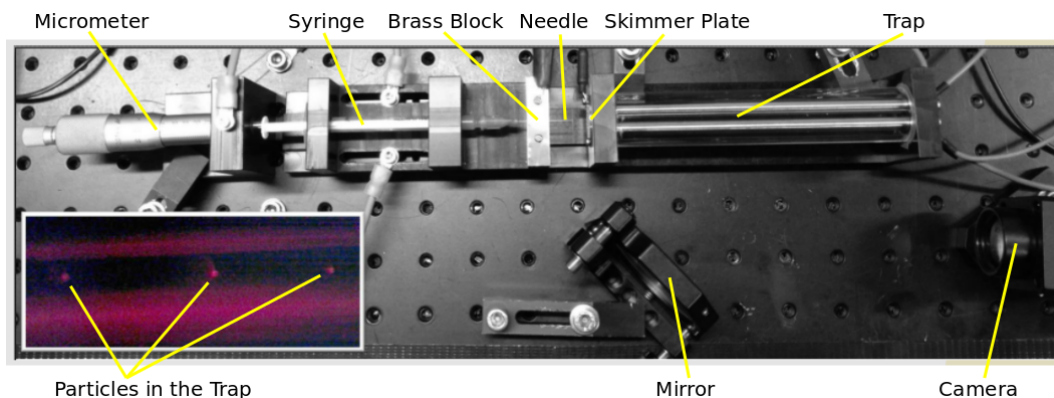

Figure 3.1: The spraying and trapping system at atmosphere.

Refer to Fig. 3.1 for a picture of the electrospray set-up. The electrospray was achieved by connecting a nonconducting syringe to a conducting needle tip, and placing these opposite a grounded plate to form a cathode anode system. This needle tip has inner diameter 200 µm and is connected to a high voltage power supply which produces up to 3 kV. The needle tip to grounding plate distance varied between 40 and 140 mm. We experimentally determined the optimum conditions for electrospray

13

to be a tip-plate distance of 100 mm, with a negative potential of 2.5 kV across the needle.
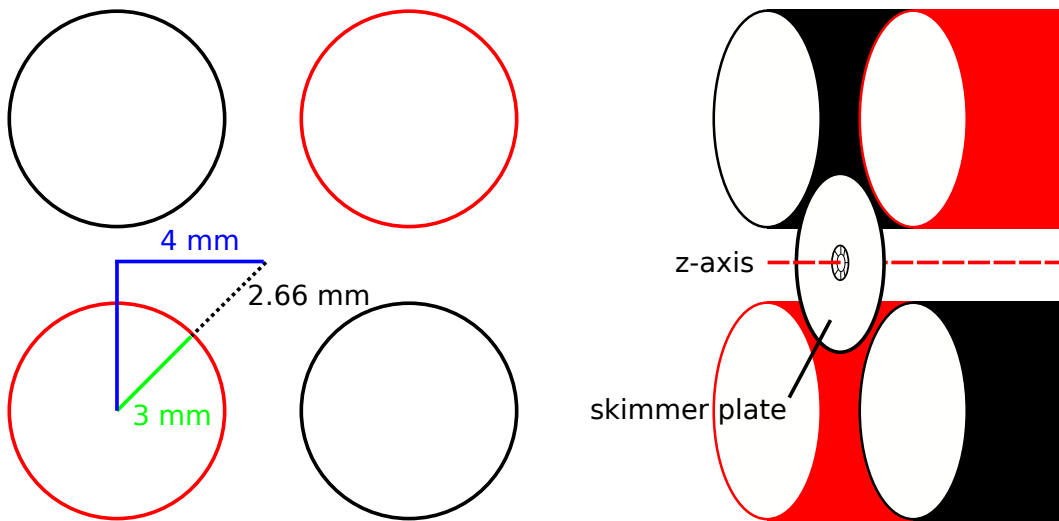
3.2 The Quadrupole Trap

Figure 3.2: Schematic of trap, front and side views.

As discussed in Sec. 2.2, a time-varying electric field can be used to trap charged nanoparticles. The trap used for this thesis consists of four stainless steel rods, 150 mm in length and radius 3 mm, with a two-axis symmetry about a central axis running lengthwise along the rods. The rods are set with 2 mm clearance from each other, giving a minimum distance of 2.66 mm between the rod surface and the central axis of the trap. See Fig. 3.2 for a schematic diagram.

The rods are set into polyoxymethylene (POM) endpieces. Both end pieces have an additional hole drilled on the central trap axis, allowing a probe laser to be aligned along this axis. The rod spacing is sufficient such that there is optical access along this axis, permitting light scattered from the nanoparticles to be collected. At one end, the rod mounting holes are drilled through the POM, allowing for electrical connections to be made to the rods. At the other end, the outside of the POM is fitted with a stainless steel plate, centred on the trap axis, with a tapered hole drilled in the middle. This skimmer plate provides the anode in the electrospray process, and the taper helps focus the spray in to the trap.

3.3   Electronics

The rods are electrically connected in diagonally opposite pairs, with one pair set to ground and the other pair connected through a voltage amplifier to a signal generator. Thus the independent variables are the frequency (Ω) and amplitude (V) of the signal produced at the signal generator. These control the frequency (ω_{trap}) and amplitude (V_{trap}) of the electric field in the trap. We operated the trap in the range between 30 and 10 kHz, and between 20 and 200 V. Using the trap stability parameters discussed in Sec. 2.3, and putting in the above values, one can see that we expect charge-to-mass ratios in the order of 1 C/kg.
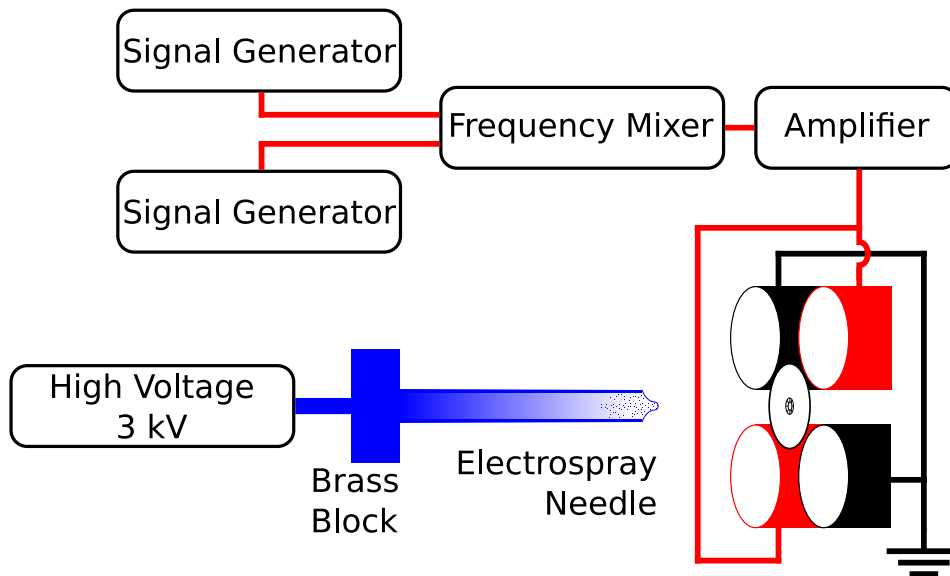

Figure 3.3: Schematic of the electronic system of the trap.
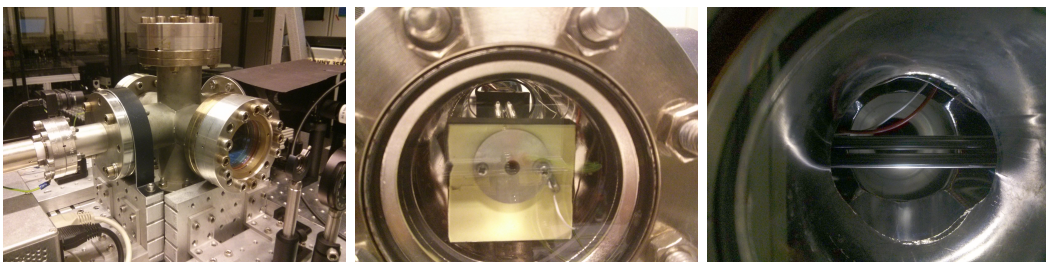
3.4   The Vacuum Chamber

Figure 3.4: The vacuum chamber, from left to right: exterior view; interior view showing the skimmer plate and trap; interior view from the imaging system point of view.

The vacuum chamber for this thesis was designed to reach a medium vacuum, or

approximately 10 Pa. It is constructed symmetrically along three orthogonal axes, which match those defined previously for the trap. It provides for optical access along all three axes, though some ports are blocked by pumping or measuring equipment. The chamber is pumped by a $5\,\mathrm{m^3/h}$ scroll pump, with a typical ultimate vacuum under 7 Pa. The pumping line includes a micrometer needle valve as well as a higher-volume valve, allowing for precision control of the flow rate of the evacuation of the chamber. Refer to Fig. 3.4 for photographs of the vacuum chamber.
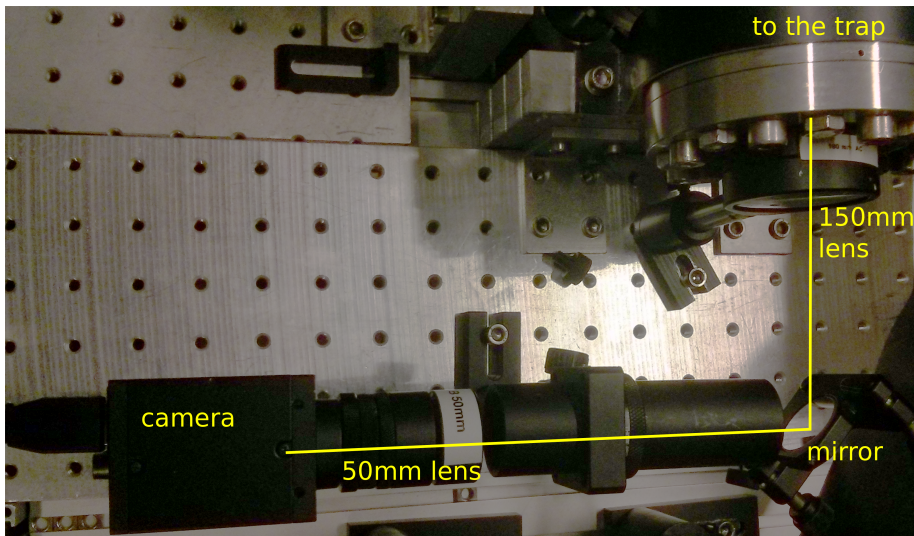
3.5   The Imaging System

Figure 3.5: The imaging system.

The imaging system for this thesis consists of two lenses, a mirror, and a camera. Due to the layout vacuum chamber, the trap is only visible from perpendicular views. The distance from trap center to viewport is 144 mm. A 150 mm focal length lens is placed just beyond this viewport, with the central axis of the trap at its focus. The subsequent optical path is adjusted to meet experimental constraints, but is always run through a lens tube to block out background light. A second lens is placed at the focal distance before the camera, as a telescope lens. Thus the magnification of the particles is based only on the ratio of the focal lengths of the lenses. The camera lens is swapped as needed based on the experiment. Refer to Fig. 3.5 for a schematic of the imaging system.

4 Trapping Gold Colloids

This section describes the work of trapping the particles, and their general behaviour in the trap under various operating conditions. Particle studies in the trap first focused on one dependent variable, the charge-to-mass ratio of the particle. This was found by keeping the amplitude of the trap, V_{trap}, fixed, and varying ω_{trap}, the frequency of the trap. At some point, the particle would be ejected from the trap. This is the point where the stability boundary described in the Mathieu equations is crossed. As demonstrated in Sec. 2.3, the point in frequency space where the stability boundary is crossed gives an upper bound on the charge-to-mass ratio. Subsequent work adds a second driving frequency, which allows us to examine a trapped particle's resonance peaks.

4.1 Trapping in Atmosphere

Trapping in standard atmosphere benefits from the fact that the correction term of the Mathieu equation, as shown in Fig. 2.5, widens the stability zone considerably. This is evident in the frequencies where particles are trapped. Due to this broadening of the stability zone, particle trapping is more simple. However, this broadening also makes it difficult to test individual parameters.

For this experiment, the V_{trap} was set near $100\,\text{V}$ and ω_{trap} was varied between 600 and $30\,\text{Hz}$. Particles are loaded into the trap, and their responses to the change in driving signal is observed as a change in their secular motion.

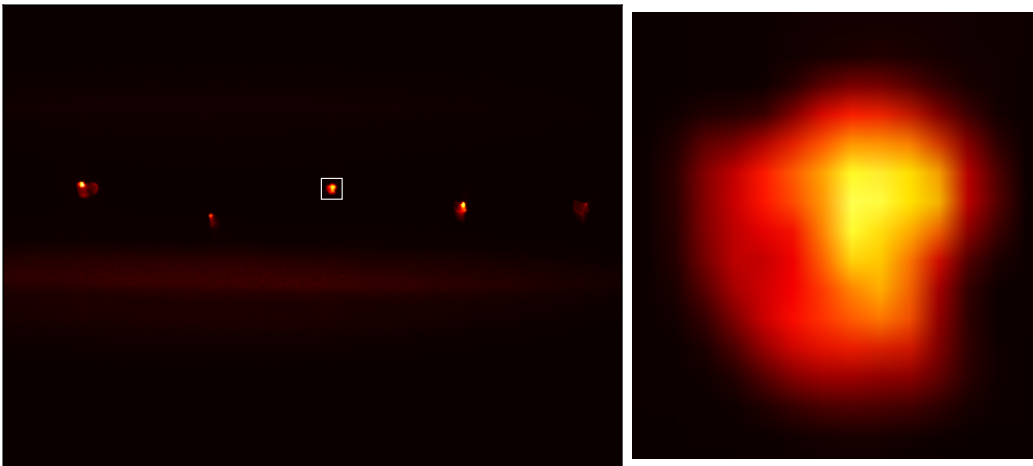**Figure 4.1:** Particles trapped at standard atmosphere
The trap is set to $V_{\text{trap}} = 109.8\,\text{V}$ and $\omega_{\text{trap}} = 500\,\text{Hz}$.
The camera is set to $60\,\text{ms}$ integrations, with a gain of $0\,\text{dB}$.

Fig. 4.1 shows particles in the trap at atmosphere. On the left side, a wide-angle

view shows five particles in the trap, with one highlighted. Note how the particles do not lie on a single axis. The low frequency of the trapping means that the particles deviate further from the trap axis. This deviation is based on their charge-to-mass ratios. Additionally, loose trapping causes the particles to be much more reactive to the atmosphere surrounding them.

On the right side, the highlighted particle is shown close up. This particle exhibits comatic aberration. This comes from an acrylic cylinder installed around the trap in an attempt to control air flow. Within the particle's coma, there is a visible brighter bar. This is the actual particle, exhibiting the secular motion about the trap axis, over the camera's integration time.

Typical trap ejection frequencies in atmosphere are between 30 and 60 Hz. This corresponds to κ damping terms which completely dominate the Mathieu equation. Thus, trapping at atmosphere is easier, due to broadened stability zones. However, precise correlation of individual parameters in the stability term to measurements of the particle's behaviour in the trap are more difficult.

4.2   Trapping in Vacuum

Trapping in vacuum benefits from the fact that the atmospheric correction is reduced, which makes experimenting with the particles more simple. The particles are not actually trapped in vacuum. Instead, they are trapped in atmosphere, as described in Sec. 4.1. Then the vacuum chamber is sealed, greatly reducing the air movement within the trap. Next, ω_{trap} is raised to 5000 Hz, which is considerably above the stability threshold for typical particles at medium vacuum pressure. Then the atmosphere is pumped out of the vacuum chamber.

The pumping must proceed carefully, so as to not eject the particles from the trap. During pump out, the particles move along the free axis of the trap, pulled along by air flow within the chamber. If the chamber is well sealed, the airflow is directed towards the center of the trap. This causes some divergence of particles from the free axis of the trap, as the particles approach each other and Coulomb repulsion causes them to buckle.

The free axis movement undergoes a qualitative change during the pump out. The particles realign to the central trap axis. This results in the particles moving along the free axis of the trap, eventually sitting a points dependant on their electrostatic repulsion from each other. The particles now form an ordered array along the trap axis, with their behaviour influencing each other such that they begin to move collectively.

In this experiment, the V_{trap} was set at 100 V and ω_{trap} was varied between 5000 and 500 Hz. The vacuum chamber pressure was typically 12.5 ± 7.5 Pa.
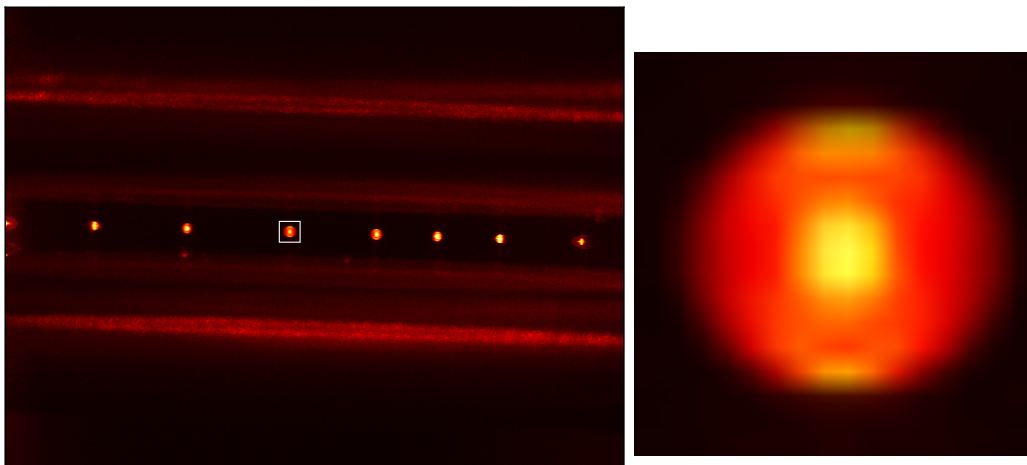
Figure 4.2: Figures of Particles in Vacuum
The pressure in the vacuum chamber is $12.5 \pm 7.5\,\mathrm{Pa}$.
The trap is set to $V_{\mathrm{trap}} = {\sim}100\,\mathrm{V}$ and $\omega_{\mathrm{trap}} = 5000\,\mathrm{Hz}$.
The camera is set to $60\,\mathrm{ms}$ integrations, with a gain of $0\,\mathrm{dB}$.

Fig. 4.2 shows two pictures of the trap in vacuum. On the left side, a wide-angle view shows many particles in the trap, with one highlighted. Notice how these particles are on-axis, due to ω_{trap} being significantly higher in vacuum.

On the right side, the highlighted particle is shown close up. The comatic aberration is significantly reduced. Additionally, note that the particles no longer have such a strong bar shaped appearance. This also comes from the trapping frequency higher in vacuum. With the κ coefficient reduced to a minor correction, the stability term q from the Mathieu equation will now accurately reflect the charge-to-mass ratio of the particle.

Fig. 4.3 shows a histogram of the charge-to-mass ratios of 262 particles. The trap fits less than forty particles at a time, and typically less than half that survive the pump out. As such, this data is constructed over separate experimental runs, and contains experimental variations. We take measurements via turning down ω_{trap} until a particle is flung from the trap, and then noting that frequency. The details of this experiment are discussed in [22].

Homogeneous nanoparticles, loaded into the trap by a uniform electrospray process, would have a reasonably uniform charge-to-mass ratio. Charge scales by the square of the particle radius, while mass scales by the cube of the particle radius. Aggregates of particles would therefore have a much wider spread in charge-to-mass ratios. Through this entire thesis work, there has been evidence that individual particles are forming aggregates. This graph confirms that the particles trapped are aggregates.

Due to the fact that aggregates would form with discrete mass steps, the charge-to-
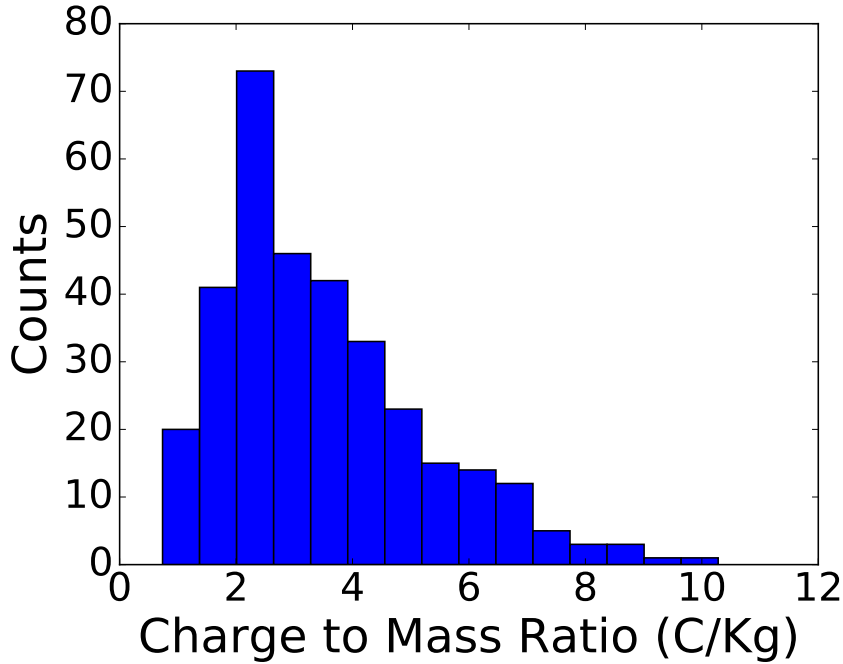
Figure 4.3: Charge-to-mass ratios for some 250 particles.

mass ratio of smaller aggregates would show these discrete steps. By taking a large amount of data, we had expected that different species of aggregate would become visible in the charge-to-mass ratio histogram. Unfortunately, the hoped-for taxonomy of aggregates did not materialize. This implies that the aggregates are large.

4.3   Resonance Peaks

A more precise measure of the charge-to-mass ratio is possible if the particle's resonant frequency response can be examined. Using a single trap frequency signal, particles are flung from the trap before they reach their resonance peaks. To study this resonance response, a second signal generator is introduced to the experiment. The signals from both generators are mixed in a purpose-built frequency mixer. For labelling purposes, the first signal is named the *trap* signal. The second signal is named the *tickle* signal [23].

Fig. 4.4 shows a schematic diagram of the frequency mixer. The mixer takes the two signals as inputs, runs both over voltage dividers, and outputs one signal to the amplifier. The amplitude of the first signal, V_{trap}, is left relatively unchanged. The amplitude of the second signal, V_{tickle}, is reduced to some 2.63% of its input value. The mixer exhibits beating if the frequencies are to close to each other. To accommodate this, the two frequencies were always kept more than $5\,Hz$ apart from
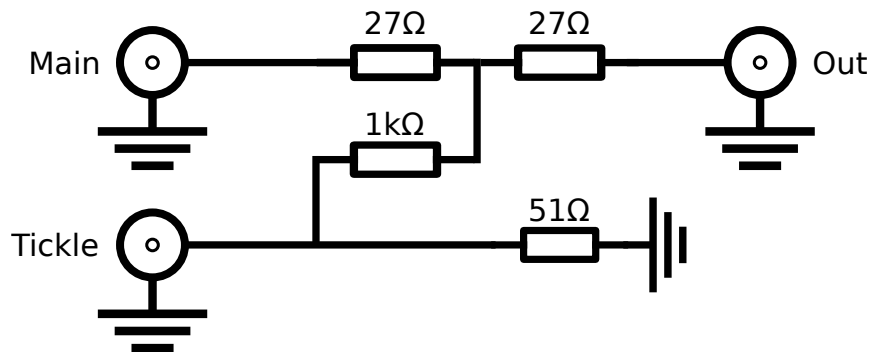
Figure 4.4: Schematic of the frequency mixer.

each other.

The introduction of the second signal allows a particle to be kept with a stable f_{trap}, but to be made to resonate by adjusting the f_{tickle} across the particle's resonant frequency. To do this, a particle is loaded into the trap, and its charge-to-mass ratio is bounded as described in Sec. 4.2. Then f_{trap} is set 10% away from this boundary, and an expectation value for f_{tickle} is calculated. With V_{tickle} set to the minimum possible, f_{tickle} is introduced and swept in frequency space over the expected value. V_{tickle} is progressively increased with each sweep until the particle responds. Once the particle becomes responsive, the sweep range is bisected, the time spent on each step of the sweep (dwell time) is doubled, and V_{tickle} is returned to the minimum. V_{tickle} is again increased until a response was noted, and the process is repeated.

Fig. 4.5 shows a particle being swept over its resonance peak. The first picture shows the particle stably trapped. The second picture shows the particle near its resonance peak. The particle's secular motion perpendicular to trap axis has increased significantly. This increase in secular motion is a measure of the resonance. By measuring increases in the secular motion, we can find the resonance peaks of a particle. The frequency of this resonance peak is a much better indicator of the charge-to-mass ratio of a particle than the frequency at which the particle is flung from the trap. This is because a particle which crosses the stability boundary, experiences an exponential increase in its instability. This exponential increase can begin quite slowly. Thus, it is quite easy to note the incorrect value for unstable boundary.

Additionally, measuring the width of the resonance peak can give information about the mass of the particle. The κ coefficient is dependent on the radius of the particle, but is insensitive to its electric charge. Thus, knowing the charge-to-mass ratio precisely, and examining the damping of the particle during the resonance sweep would give some hints as to its mass.
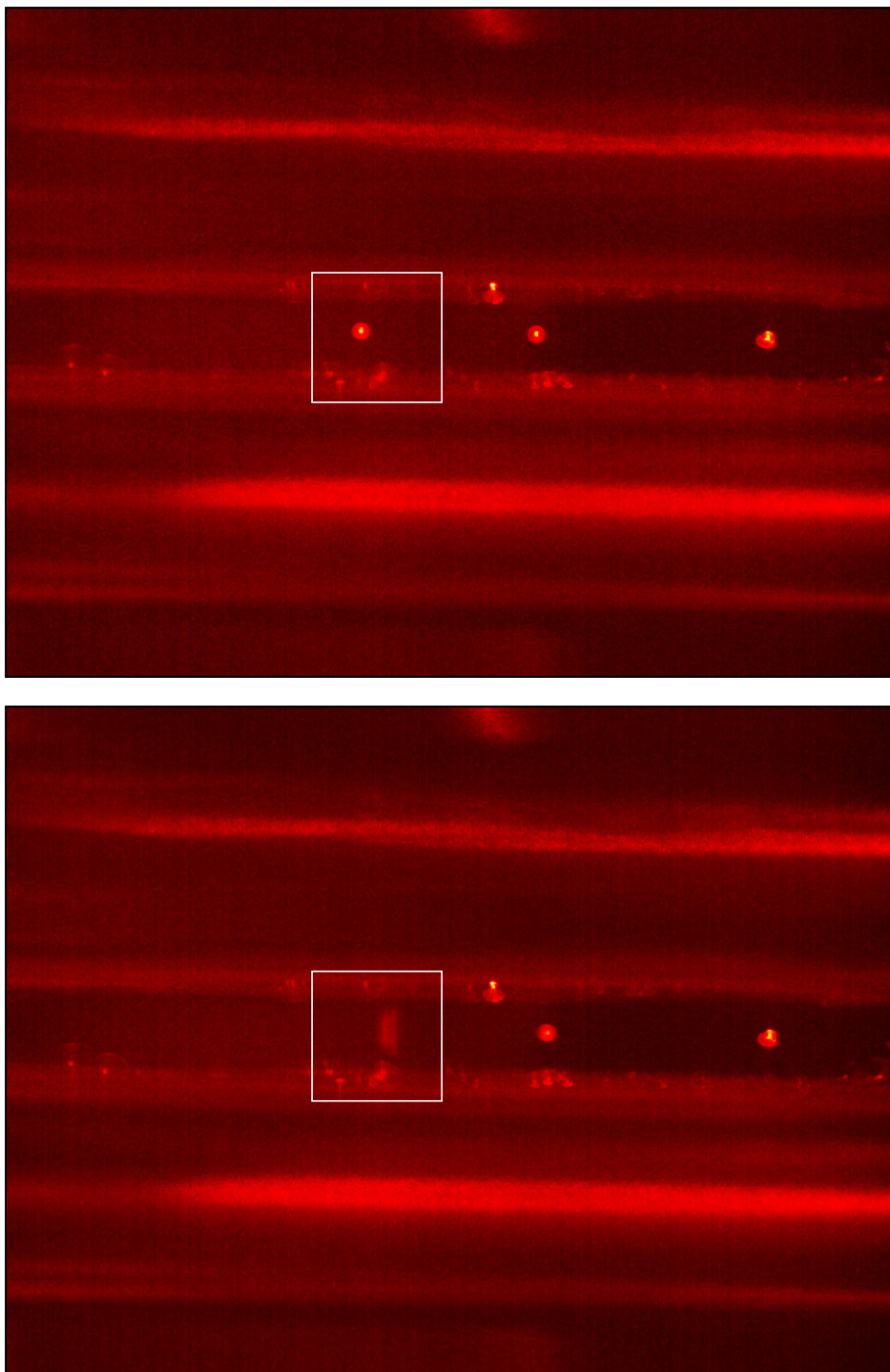
21

Figure 4.5: Figures of a Particle Resonating
The pressure in the vacuum chamber is $12.5 \pm 7.5\,\text{Pa}$.
The trap is set to $V_{\text{trap}} = {\sim}100\,\text{V}$ and $\omega_{\text{trap}} = 5000\,\text{Hz}$.
The camera is set to $60\,\text{ms}$ integrations, with a gain of $0\,\text{dB}$.

22

5   Analysis and Results

This section describes the behaviour of the particles in the trap under the influence of two trapping frequencies, as described in Sec. 4.3. It focuses on two different examples of nonlinear behaviour, in the frequency domain and the time domain.

Resonating particles appear on the camera as bars, due to their increased secular motion. The strength of their resonance can be measured as the length of this bar. By taking images of the particle periodically, the progression of the resonance can be tracked over time. By setting the signal generator to make a frequency sweep, the progression of the resonance can also be tracked in the frequency domain.

5.1   Data Analysis

Refer to Sec. 3.5 for a more complete discussion of the imaging system. The recording settings of the camera are adjusted from experiment to experiment to optimize the acquired data. The sets of images are analysed after the fact, using the OpenCV software library and the Python programming language.
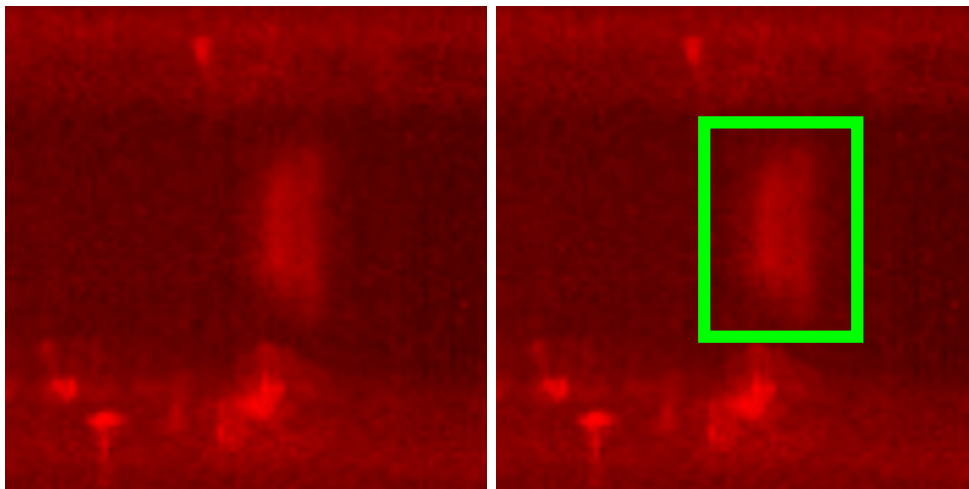

Figure 5.1: A particle near its resonance peak, and the region of interest box taken by the analysis software.

Particles at their resonance peaks become difficult to spot, but they remain on the trap axis. This software looks for local maxima in intensity along the trap axis. When the software identifies the region in which the particle is, and extracts this region from the rest of the image. It takes a comparably sized region from a different part of the image, to perform a background subtraction. Fig. 5.1 shows a close up of the particle near its resonance peak, and the region of interest taken by the software.
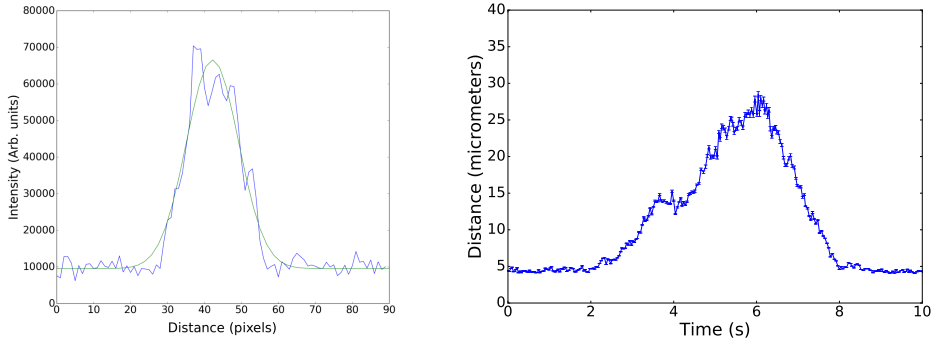
Figure 5.2: Images showing the data analysis process
The right image shows the integration of the region of interest box, with a Gaussian fit
The left image shows the width of these fits for every frame of a ten second video.

Next, the software integrates the region of interest along the z-axis, to negate the free movements the particles make in this direction. This produces a one-dimensional array, which records the intensity of the particle's motion away from the trap axis. A Gaussian function is fitted to the data by a fitting program. The fitted width of this Gaussian function is taken as a measurement of the particle's movement away from the trap axis. This width is then converted from pixels to micrometers via the pixel pitch of the camera and the lens choices for the experiment. By performing this fit on every frame of a video, we can create a graph of the changes in a particle's secular motion over time. Fig. 5.2 shows the steps of the data analysis process.

The graphs presented in this section are made up of data points acquired in this way. In the frequency domain, the signal generator creating the f_{tickle} signal is made to sweep through a defined range of frequencies, with a defined dwell time. The progression in the time domain is relatively simple to keep ordered.

5.2   Frequency Domain

To perform this experiment, the resonant frequency of the particle is identified via the method described in Sec. 4.2. When the sweep range has been reduced to a manageable size, the dwell time of the sweep and the amplitude of f_{tickle} are balanced to produce a good result. Then the direction of the sweep is reversed, while the other parameters are kept the same. These two sweeps are then compared.

In the frequency domain, the particle's response is limited by the dwell time of the sweep. The particle's calculated relaxation time is on the order of $0.5\,\text{s}$. To accommodate this, the sweeps in this experiment are run at $1\,\text{Hz/s}$.

Fig. 5.3 shows f_{tickle} against the particle secular motion. The two graphs are sweeps over the same particle, with equivalent experimental conditions. The right image
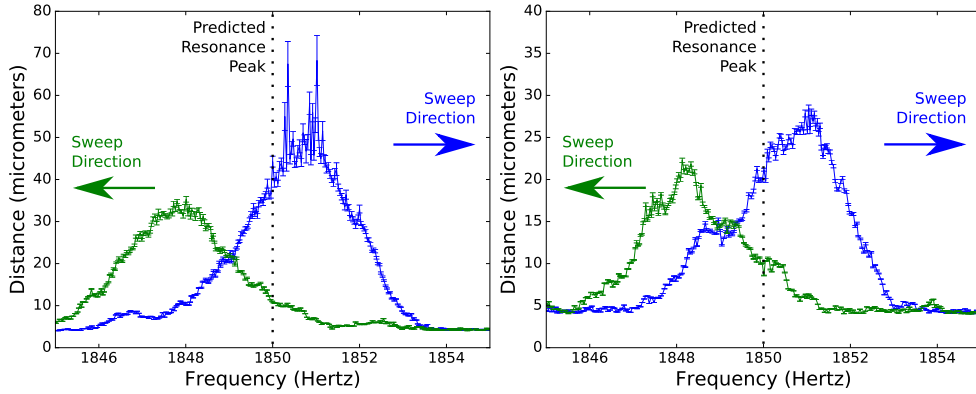
Figure 5.3: Particle secular motion, under the influence of f_{tickle} swept over resonance. Both images show the same particle, with the same conditions in the trap except for V_{tickle}. The left image shows the particle resonance with $V_{\text{tickle}} = 34.0\,\text{mV}$. The right image shows the particle resonance with $V_{\text{tickle}} = 33.9\,\text{mV}$.

was made with V_{tickle} set $126\,\mu\text{V}$ less than the left one. Note that the y-axis of these graphs is not the same.

Each graph shows two sweeps each, the blue from lower frequency to high and the green from high frequencies towards low. The theoretically calculated resonance peaks is $f_{\text{tickle}} \approx 1850\,\text{Hz}$.

These graphs demonstrate a shift of the resonance peak. This implies a delay, or hysteresis, in the particle's response to the frequency sweep. This hysteresis is related to the direction of the frequency sweep. The graphs also show complex structure in the resonance peak. The complexity within the structure changes both with the direction of the sweep, as well as its intensity.

The observed hysteresis in the resonance peak, and the attendant differences in the structure of the peak, indicates nonlinearity in the response model.

5.3   Time Domain

Sweeping over the resonance peak indicates that the particles behave nonlinearly. By giving the particles longer to come to resonance, smaller driving amplitudes can be used. The goal of this experiment was to find a driving amplitude small enough to discover some repeatability in the resonance response.

To perform this experiment, the resonant frequency of a particle in the trap is identified via the method described in Sec. 4.2. The sweeping is turned off, with f_{tickle} is set to the resonant frequency, and V_{tickle} set to the minimum. We then raise V_{tickle} until the particle begins to show additional secular motion. The particle is then stabilized again, by removing the influence of f_{tickle}. Lastly, using values for V_{tickle} less than

initial one, the particle's response over longer periods of time is observed.

Typically, a particle would still be to responsive, even at the minimum possible values for V_{tickle}. In this case, the value of f_{trap} would be adjusted to be further away from the stability boundary. The experiments begin with $f_{\text{trap}} = 110\%$ of the stability boundary, and can be pushed as far as 130% before the system becomes unmanageable. Fig. 5.4 shows a particle being made to resonate in this way. The timeline of this resonance is approximately $15\,\text{s}$.
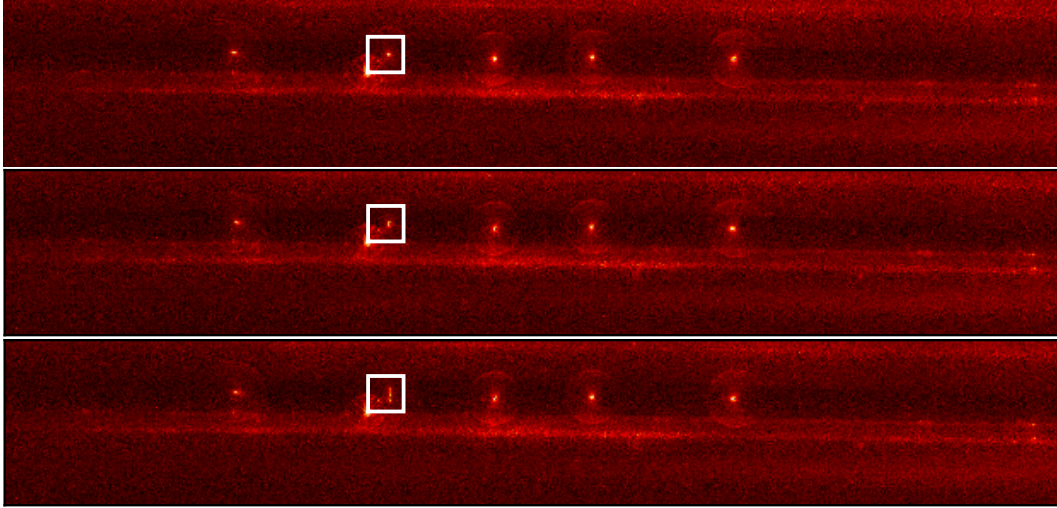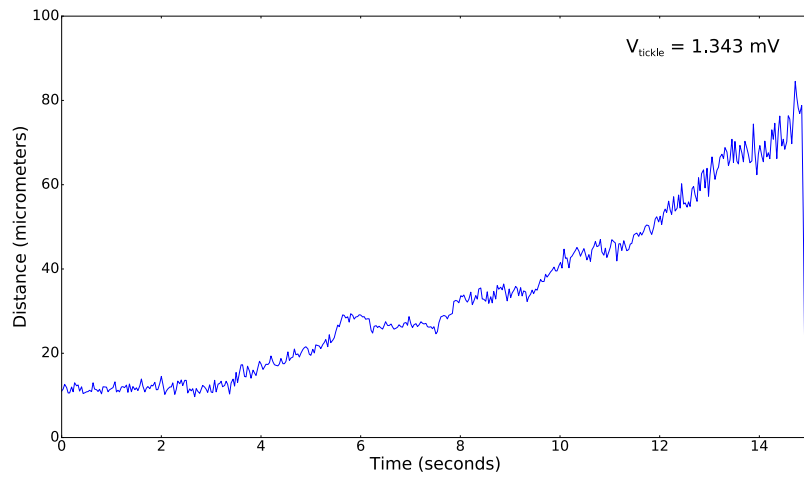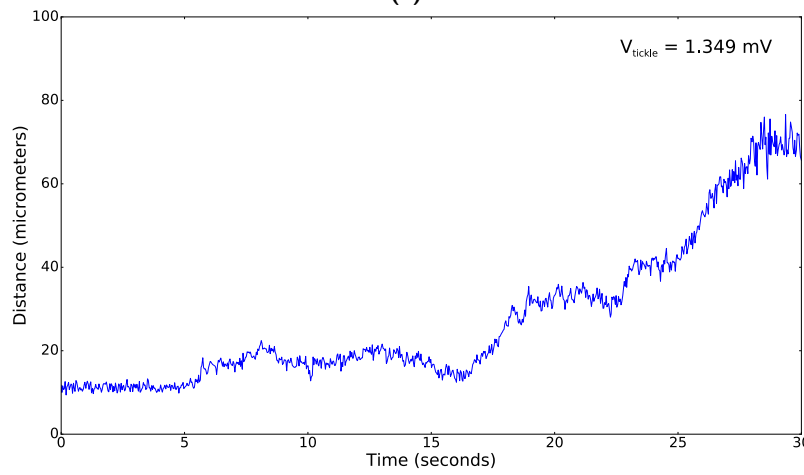

Figure 5.4: Particle secular motion under the influence of a stable perturbing signal.
Here f_{trap} is set to $1750\,\text{Hz}$, which is approximately 133% of the stable value,
and f_{tickle} is fixed at $660.9\,\text{Hz}$, with amplitude $1.355\,\text{mV}$.
The pressure in the chamber is $7.2\,\text{Pa}$.

Fig. 5.5 shows the same particle as Fig. 5.4, but at three different values of V_{tickle}. Note that the time scale on the x-axis of the graphs changes significantly. Fig. 5.5a shows the particle generally increasing in motion over a period of $15\,\text{s}$. Fig. 5.5b shows the particle exhibiting considerably more complex motion, though it does still eventually increase, and reaches the same level of secular motion at $25\,\text{s}$. Fig. 5.5c shows the particle coming in and out of resonance, and still not reaching a stable condition after $65\,\text{s}$. These graphs represent a difference of $6.3\,\mu\text{V}$ in the perturbing signal, the minimum the system was able to produce. At this point, the signal to noise ratio of the amplifier is a significant factor in the tickle signal.
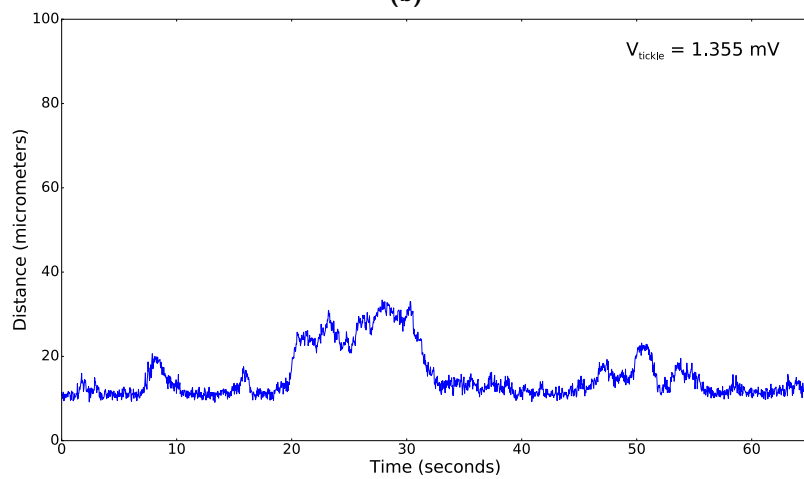
The complexity of the increase in the particle's secular motion, and the sensitivity the particle has to its experimental conditions, imply there is a strong nonlinearity in the response model.

26

Figure 5.5: Secular motion under the influence of a stable V_{tickle}. Refer to Fig. 5.4 for the experimental details of the trap.

6   Conclusion, Discussion and Outlook

In this thesis we have demonstrated the use of a quadrupole trap to contain and study gold nanoparticles. Trapping was investigated under different atmospheric conditions, and procedures were developed for stable, long term trapping in a medium vacuum. We used frequency sweeping to establish charge-to-mass ratio values for statistically significant numbers of particles, and identified from this that the particles were aggregating. We introduced a second signal to the trapping system, and used this to bring the particles near their resonant frequencies in a stably trapped fashion. Thus we were able to study the properties of the particles near resonance as well.

We attempted several variations on dilution and filtration of the colloidal suspension prior to the electrospray, and found these to have negligible effects on the aggregates in the trap. We identified that the aggregation therefore results from during or after the electrospray. Additionally, the pump out of the vacuum chamber is a mass selective process, which results in only the more larger aggregates being left in the trap. Finally, particles in the trap were observed to behave in strongly nonlinear fashions. It is likely that these effects are related to the particles in the trap being aggregates, rather than single colloids.

We recommend that further consideration be given to the aggregation of the colloids. Establishing the mass of the trapped particles is essential prior to ablation, and is a major stumbling point other physical investigations as well.

A technique called polarimetry could be used to identify the mass of the particles. Polarizing the illuminating laser beam would also polarize the light scattered by the particles within the trap. By varying polarization of the incoming laser beam, and measuring the intensity of the scattered light through a known polarizing filter, one can make a graph of the preferential scattering for various polarizations. By doing this with two different frequencies of incoming light, one is able to compare the two graphs and identify the mass of the particle.

Also of note the Coulomb crystal. As described in Sec. 4.2, particles in the trap interacted visibly with one another. This interacting group of particles can be treated as a Coulomb crystal. The distances between these particles is related to their electric charge. From the charge, and the charge-to-mass ratio, it is possible to discover the mass of the particles.

The particle's response in the presence of a potential wall could also be used to identify its charge, and thus its mass. Potential walls could be created locally via segmenting the trap. Using several of these segments, particles could also be moved about the free axis of the trap as needed. This would be extremely useful for bringing particles into the focus of a laser beam.

Once the particles in the trap have been characterized, we can proceed with ablation.

7 Acknowledgements

This thesis was made possible by a legion of people who counselled and supported me. To thank them all would be impossible here, so I shall restrict myself to those people in the Utrecht physics department. That being said though, I must make special mention of my mother and sister, for their unfailing support and unconditional love. They are the rock upon which I build my church.

I owe a tremendous amount to Dr Dries van Oosten, for his uncanny ability to cut straight to the heart of a problem, his tremendous enthusiasm for finding an applicable solution after, and his willingness to put up with me when I wasn't doing either of those things as quickly as he would have liked me to. It is a pleasure and a joy to work with someone who creates a space for clever people to do clever things.

Dolfine Kosters was a boon at the start of my thesis, and signposted the early problems for me clearly and concisely. I would never have been able to accomplish as much as I did without her shoulders to stand on.

Javier Hernandez was equally a boon at the end of my thesis, when I had lost sight of the forest for all the trees. He pushed me to elucidate my work better than I ever would have on my own, and the clarity of this thesis is thanks in large part to him.

I owe a tremendous amount to the PhD students: Sebastian, Arjon, Sandy and Ole. Wise heads all and wise counsel they provided me. The technical staff of the Ornstein Laboratorium literally built my trap for me; I would not have been able to accomplish this thesis without Paul, Fritz, Dante and Cees. They also provided the whole group with some much-needed realism, for when we got a bit to crazy. My labmates can not be acknowledged enough: Gordian, Robbert, Jasper, Marcel, and Anne. I know the bass bumps loud sometimes but y'all put up with it like champs. It was inspiring to see you blossom both in the lab and out. One can only hope that the contributions we made to each other more than make up for all the shenanigans. I'd also like to acknowledge the master students not in my lab, Karindra and Kostas, for being crucial parts of the social atmosphere of the group.

I'd like to thank the Cold Atoms group, our section mates and compatriots. Prof Peter van der Straten runs a tight ship, and one can see it in his students. Koen, Qiao, Jasper and Broos contributed insights at the whiteboard, smashes at the ping pong table, and endless discussions about music.

The nanoLINX group of Prof Mosk and Dr Faez joined us late during my time at the Ornstein, but I can already tell they'll be a good fit. The borrels have only gotten better since their arrival, and the work will presumably do the same.

Lastly, I'd like to thank the coffee machine, and BBC One's Essential Mix archive. I'd never have made it without the external stimuli.

29

References

[1] N. Christofilos, *Focusing system for ions and electrons and application in magnetic resonance particle accelerators*, Privately printed report (1950)

[2] E. D. Courant, M. S. Livingston, and H. S. Snyder, *The strong-focusing synchrotona new high energy accelerator*, Physical Review **vol. 88**, no. 5, p. 1190 (1952)

[3] W. Paul and H. Steinwedel, *Notizen: Ein neues massenspektrometer ohne magnetfeld*, Zeitschrift für Naturforschung A **vol. 8**, no. 7, pp. 448–450 (1953)

[4] G. Stafford, P. Kelley, and D. Bradford, *Advanced ion trap technology in an economical detector for gc*, American Laboratory **vol. 15**, no. 6, p. 51 (1983)

[5] M. Scholten, *Experiments on ablation of dielectrics on gold, and water*, Master's thesis, Utrecht University, the Netherlands (2016)

[6] J. Clarijs, *Femtosecond laser nanoablation of glass surfaces and their self-scattering effects*, Master's thesis, Utrecht University, the Netherlands (2016)

[7] G. Zomer, *Self-scattering of gold nanoparticles under femtosecond laser ablation conditions*, Master's thesis, Utrecht University, the Netherlands (2016)

[8] B. C. Stuart, M. D. Feit, S. Herman, A. Rubenchik, B. Shore, and M. Perry, *Nanosecond-to-femtosecond laser-induced breakdown in dielectrics*, Physical review B **vol. 53**, no. 4, p. 1749 (1996)

[9] B. N. Chichkov, C. Momma, S. Nolte, F. Von Alvensleben, and A. Tünnermann, *Femtosecond, picosecond and nanosecond laser ablation of solids*, Applied Physics A **vol. 63**, no. 2, pp. 109–115 (1996)

[10] A. D. McNaught and A. D. McNaught, *Compendium of chemical terminology*, vol. 1669, Blackwell Science Oxford (1997)

[11] L. Rayleigh, *Xx. on the equilibrium of liquid conducting masses charged with electricity*, The London, Edinburgh, and Dublin Philosophical Magazine and Journal of Science **vol. 14**, no. 87, pp. 184–186 (1882)

[12] L. Loeb, A. Kip, G. Hudson, and W. Bennett, *Pulses in negative point-to-plane corona*, Physical Review **vol. 60**, no. 10, p. 714 (1941)

[13] S. Earnshaw, {*On the nature of the molecular forces which regulate the constitution of the luminiferous ether*}, Trans. Camb. Phil. Soc **vol. 7**, pp. 97–112 (1842)

[14] H. G. Dehmelt, *Radiofrequency spectroscopy of stored ions i: Storage*, Advances in Atomic and Molecular Physics **vol. 3**, pp. 53–72 (1968)

[15] R. E. March, *Quadrupole ion traps*, Mass spectrometry reviews **vol. 28**, no. 6, pp. 961–989 (2009)

[16] T. Hasegawa and K. Uehara, *Dynamics of a single particle in a paul trap in the presence of the damping force*, Applied Physics B **vol. 61**, no. 2, pp. 159–163 (1995)

[17] É. Mathieu, *Mémoire sur le mouvement vibratoire d'une membrane de forme elliptique.*, Journal de mathématiques pures et appliquées **vol. 13**, pp. 137–203 (1868)

[18] G. G. Stokes, *On the effect of the internal friction of fluids on the motion of pendulums*, vol. 9, Pitt Press (1851)

[19] E. Cunningham, *On the velocity of steady fall of spherical particles through fluid medium*, Proceedings of the Royal Society of London. Series A, Containing Papers of a Mathematical and Physical Character **vol. 83**, no. 563, pp. 357–365 (1910)

[20] C. Davies, *Definitive equations for the fluid resistance of spheres*, Proceedings of the Physical Society **vol. 57**, no. 4, p. 259 (1945)

[21] N. Kosters, *Isolation of single gold nanoparticle*, Tech. Rep., Universiteit Utrecht (2013)

[22] B. van Assen, *Neerslagstatistiek van goud in vacuum*, universiteit Utrecht (2015)

[23] R. E. March and J. F. Todd, *Practical Aspects of Trapped Ion Mass Spectrometry, Volume V: Applications of Ion Trapping Devices*, CRC Press (2016)